An interpretation of Australian rainfall projections

G. Shi,[1] J. Ribbe,[1] W. Cai,[2] T. Cowan[2]

Ge Shi, CSIRO Atmospheric Research, PMB 1, Aspendale, Victoria 3195, Australia. (ge.shi@csiro.au)

[1]Department of Biological and Physical Sciences, University of Southern Queensland, Queensland, Australia.
(ge.shi@csiro.au)

[2]CSIRO Marine and Atmospheric Research, PMB 1, Aspendale, Victoria 3195, Australia.

The majority of climate models project a winter rainfall reduction over south-eastern Australia (SEA), while some show a tendency for a summer rainfall increase. The dynamics for these rainfall changes are not clear. Using outputs from a participating model, we show that a summer rainfall increase is consistent with a large Tasman Sea warming promoting convection, and an upward trend of the Southern Annular Mode (SAM) promoting onshore flows; these processes dominate over a rainfall decrease from an El Niño-like warming pattern. In winter, similar effects from a Tasman Sea warming and an upward SAM trend operate along Australia's east coast, however, the rain-reducing impact of an Indian Ocean Dipole-like warming pattern dominates. In both seasons, the upward SAM trend causes a rainfall reduction over southern Australia. Summer rainfall over north-western Australia is projected to decrease, due to an unrealistic relationship with the El Niño-Southern Oscillation. Possible uncertainties are discussed.

1. Introduction

The majority of the climate models used in the Intergovernmental Panel on Climate Change (IPCC) Fourth Assessment Report (AR4) project a decrease in winter rainfall (June - August, JJA) over SEA (Fig. SPM7, *Alley et al.* [2007]), while some show a tendency for a rainfall increase in summer (December - February, DJF). However, the governing dynamics are not clear. One associated feature is the warming rate in the Tasman Sea that is fastest of the Southern Hemisphere [*Cai et al.*, 2005a], due to a poleward intensification of the East Australian Current (EAC). We will investigate how the Tasman Sea warming contributes to SEA rainfall changes.

Climate variability in SEA is affected by three engines: El Niño-Southern Oscillation (ENSO) [*Nicholls et al.*, 1996], the Indian Ocean Dipole (IOD) [*Saji et al.*, 1999;*Ashok et al.*, 2003; *Cai et al.*, 2005b] and the SAM [*Cai and Cowan*, 2006; *Meneghini et al.,* 2007]. The impact of ENSO occurs mainly in spring and summer with anomalously low rainfall during an El Niño; the IOD influences the spring and autumn rainfall with an anomalously low sea surface temperature (SST) in the eastern pole associated with decreased rainfall throughout SEA; and a positive SAM phase with an increasing mean sea level pressure (MSLP) in the midlatitudes tends to increase SEA rainfall, although it reduces rainfall to the west including south-west Western Australia (SWWA).

We investigate if the projected climate change is consistent with teleconnections associated with the three engines, in addition to a Tasman Sea warming, and how the response of these engines to climate change contributes to the seasonal difference in rainfall projections.

2. Model and experiments

The CSIRO "Mark 3" climate model (Mk3) runs without flux adjustments, and is an IPCC-AR4 contributing member. It simulates a well structured SAM trend [*Raphael and Holland*, 2006]. Here we use a 300-year control simulation to examine the rainfall teleconnections. We then examine outputs from four climate change experiments, following the A2 (two experiments), A1B, and B1 scenarios all incorporating a CO_2 forcing, direct effect of sulfate aerosols and ozone depletion [*Cai et al.*, 2005a], to assess the response of climate drivers and interpret rainfall changes in terms of their response. We examine the mean changes over the period 2055-2085 averaged over the four climate change experiments from a control climate.

3. Summer and winter rainfall changes

The Mk3 ensemble average of rainfall changes is similar to the IPCC-AR4 median projection, apart from an increase in SEA summer rainfall. The summer rainfall increase with the highest changes along the eastern coast (Fig. 1a) translates to some 10-20% increase (Fig. 1b). The large-scale pattern features a band of decreasing rainfall centered south of Australia at 45°S. By contrast, SEA winter rainfall decreases by up to 10%, displaying a zonal strip of decline with maximum reduction over southern Australia including SWWA (Figs. 1c and 1d). This decline is punctuated by an increase over the Tasman Sea. Other features include a reduction in both seasons over north-west Australia (NWA), where there is little consensus from the IPCC-AR4 models.

4. Teleconnections with climate drivers

We first examine the relationship between SEA rainfall (140°E-155°E, 32°S-38°S) and circulation fields in the control experiment. The influences from the three engines plus the Tasman Sea temperature are evident (Figs. 2a and 2d). A La Niña-like SST pattern in both seasons (Figs. 2b and 2e), a negative IOD phase with a warm pole in the eastern Indian Ocean (EIO) in winter (Fig. 2e), and a regional SAM-like pattern, particularly in summer (Fig. 2c), are conducive to a rainfall increase. In summer, this increase is linked with anomalous on-shore flows toward the east coast, geostrophically balanced by MSLP anomalies (Fig. 2c), and with an anomalously high Tasman Sea temperature (Fig. 2b). In winter, there is a strong influence from flows extending from the EIO (Fig. 2f).

However, significant seasonal differences exist. The influence by EIO SST is weaker in summer (Figs. 2b and 2e); the summer MSLP pattern (Fig. 2c) resembles the SAM pattern, but not so in winter. These differences reflect the varying importance of the three engines and the Tasman Sea temperature, as will be explored below.

4.1. Tasman Sea temperature

A correlation between east coast SST anomalies (averaged over 150°E-155°E, 32°S-38°S) with rainfall (Fig. 3a) and SST (Fig. 3b) fields reveals that an anomalously high summer SST "hugging" the coast is favourable to a SEA rainfall increase, extending from the coast further inland. In winter, the impact is weaker and more confined to area off the coast (Figs. 3g and 3h). This difference is consistent with the feature that in summer the subtropical ridge is furthest to the south, and SEA is impacted by episodic easterlies events; in winter, the strong climatological westerlies aloft ensure that the impact is predominantly downstream. A correlation between Tasman Sea temperature and circulation

fields shows that a higher temperature promotes convection, cloud formation, and rainfall. Thus a warm Tasman Sea is conducive to SEA rainfall in summer, but mainly off the coast in winter.

4.2. ENSO

The Mk3 suffers from a common deficiency in the equatorial Pacific Ocean: the climatological cold tongue, the western Pacific warm pool, and the rising branch of the Walker circulation all extend too far west. Further, the cold tongue is too narrow and equatorially confined. As a consequence, ENSO anomalies along the equatorial Pacific display similar spatial features (Figs. 3d and 3j). The unrealistic warm pool position leads to an unrealistic ENSO-NWA rainfall relationship: in summer an El Niño is associated with low rainfall over NWA as well as north-east Australia (Fig. 3c). In reality, ENSO influences eastern and north-east Australia. Furthermore, the influence on SEA summer rainfall is rather weak due to the narrow extent of Pacific SST anomalies. By contrast, the influence in winter is strong (Fig. 3i), due to the unrealistic feature that all IODs in the model are linked to El Niño events [*Cai et al.*, 2005b]. The weak summer ENSO-SEA rainfall relationship and the strong winter IOD-rainfall teleconnection significantly contribute to the seasonal difference in rainfall projections.

4.3. Indian Ocean variability

Correlation analysis is conducted between a time series of the first mode of empirical orthogonal function (EOF1) of Indian Ocean (IO) SST anomalies with grid point rainfall (Figs. 3e and 3k) and SST anomalies (Figs. 3f and 3l). In summer, EOF1 is driven by ENSO [*Chambers et al.*, 1999]: easterly anomalies due to El Niño superimposing on the

mean westerly winds reduce the latent heat flux and yield a basin-scale warm anomaly (Fig. 3f). Thus, the rainfall correlation pattern reflects that associated with ENSO, with an unrealistically strong influence on NWA rainfall (Fig. 3e). In winter, EOF1 represents the matured phase of the model IOD (Fig. 3l), the majority of which peak 6 months after a matured El Niño [*Cai et al.*, 2005b]. A band of rainfall teleconnections that extend from the EIO to SEA are far stronger than observations (Fig. 3k).

4.4. The SAM

The relationship of the SAM with circulation fields (Fig. 4) shows that on interannual time scales, the midlatitude center of the SAM, defined as the EOF1 of MSLP anomalies, is located near 45°S in summer, and further north in winter (Figs. 4c and 4f). A positive summer SAM with an anomalously high midlatitude MSLP is conducive to SEA rainfall, including the east coast (Fig. 4a). The associated SST anomaly pattern and on-shore flows (Figs. 4b and 4c) resemble those shown in Figs. 2b and 2c. Although a long-term upward SAM trend generates a stronger EAC and a large Tasman Sea warming, the time scale involved for Rossby waves to transverse the Pacific, at 40°S, is 15-20 years [*Qiu and Chen*, 2006]. The anomalies shown here do not reflect this, but represent variations on shorter time scales: a high MSLP reduces cloud cover, and increases radiation into the ocean, generating warming anomalies.

A positive winter SAM has a spatially non-uniform impact on SEA rainfall: the associated onshore air flows (Fig. 4f) increase rainfall along the east coast, whereas the midlatitude high MSLP reduces rainfall over the southern-most tip of Australia, includ-

ing SWWA (Fig. 4d). The associated SST anomalies (Fig. 4e) are small and are located to the north of the summer anomalies (Fig. 4b).

5. Interpretation of rainfall changes

We now describe the circulation changes relative to the control climate and interpret the rainfall changes in terms of teleconnections with climate drivers. The Indo-Pacific warming pattern is El Niño-like in terms of the zonal SST gradients over the equatorial eastern IO and western Pacific (Fig. 5a). Further, a SAM-like trend is generated in both seasons (Figs. 5b and 5e, compared with Figs. 4c and 4f); the associated change in the wind stress curl drives a stronger and poleward shifting EAC, generating a large warming rate in the Tasman Sea (Figs. 5a and 5d).

5.1. Summer rainfall change

The SAM-like change and a Tasman Sea warming are conducive to a summer rainfall increase over the Tasman Sea and SEA, whereas the El Niño-like pattern contributes to a reduction. The net result is a rainfall increase, because of the weak effect of the El Niño-like pattern. This is further illustrated by an increase in the longwave radiation at the top of the atmosphere indicating an enhanced convection (not shown) and a reduced surface net shortwave radiation over SEA (Fig. 5c). As discussed in section 4.2, the model ENSO impact on SEA summer rainfall is too weak; this might indirectly lead to a greater rainfall increase than otherwise expected. Over NWA, the El Niño-like pattern contributes to a rainfall decrease, with increasing incoming surface net shortwave radiation extending from the EIO (Fig. 5c) because of the unrealistic model ENSO-NWA rainfall relationship.

5.2. Winter rainfall change

According to the winter SAM-rainfall relationship (Fig. 4), an upward SAM trend will lead to a rainfall reduction over southern Australia and SWWA, consistent with the IPCC-AR4 results [*Alley et al.*, 2007]. An upward SAM trend (Fig. 5e) and the Tasman Sea warming (Fig. 5d) should contribute to a rainfall increase along the east coast, both off shore and further inland over much of SEA. Off shore, the increase is rather conspicuous due to the large Tasman Sea warming. However, throughout much of inland SEA, rainfall actually decreases. This is overwhelmingly due to a strong offsetting impact from the tropical Indo-Pacific, where the warming pattern is IOD- and ENSO-like. However, the drying effect from the SAM has some influence. The strong effect from the IOD-like pattern is seen in an increased surface net shortwave radiation extending from the EIO to SEA (Fig. 5f).

The IOD-like warming pattern is linked to the model monsoon changes. As in other models, the Asian monsoons increase under a warming climate, contributing to a weaker EIO warming. A strengthening monsoon despite an El Niño-like pattern is in contrast to their historical relationship, in which El Niño events are generally associated with weaker monsoons. In our model, the IOD-like warming pattern is caused by an increase in the south-easterly winds over the EIO as a result of a greater transient greenhouse warming of the Eurasian landmass than that over the ocean, as simulated in other models [*Ashrit et al.*, 2001].

6. Conclusions

The majority of IPCC-AR4 global climate models project a reduction in winter rainfall over SEA, while some show a summer rainfall increase. We find that the summer rainfall increase is consistent with a large Tasman Sea warming promoting convection, and an upward trend of the SAM promoting air flows towards the SEA coast; both processes would appear to dominate over a rainfall decrease resulting from an El Niño-like warming pattern. In winter, a Tasman Sea warming and an upward SAM trend operate predominantly along Australia's east coast, but the strong rain-reducing impact of an IOD-like warming pattern dominates. To the west, the drying effect from the upward SAM trend also contributes to the winter rainfall reduction. Rainfall over NWA is projected to decrease, due mostly to an unrealistic ENSO-NWA rainfall relationship. Because the net rainfall change results from several reinforcing and offsetting teleconnections with the response of climate drivers, it is crucial that the relative importance of these drivers and their impacts are realistically simulated. Any future changes could lead to a shift in the direction of rainfall projections. Thus our results highlight the importance of a realistic simulation of ENSO and the IOD and their teleconnections with Australian rainfall in reducing the uncertainty of climate projections.

Acknowledgments.

We thank the reviewers for their positive comments. W. Cai and T. Cowan are supported by the Australian Greenhouse Office.

References

Alley, R., et al., (2007), Climate Change 2007: The Physical Science Basis. Summary for Policymakers. Contribution of Working Group 1 to the Fourth Assessment Report of the IPCC. *18* pp.

Ashrit, R. G., K. R. Kumar, and K. K. Kumar (2001), ENSO-monsoon relationships in a greenhouse warming scenario. *Geophys. Res. Lett.*, *28*, 1727–1730.

Ashok, K., Z. Guan, and T. Yamagata (2003), Influence of the Indian Ocean Dipole on the Australian winter rainfall, *Geophys. Res. Lett.*, *30*, 1821, doi:10.1029/2003GL017926.

Cai, W., and T. Cowan (2006), SAM and regional rainfall in IPCC AR4 models: Can anthropogenic forcing account for southwest Western Australian winter rainfall reduction? *Geophys. Res. Lett.*, *33*, L24708, doi:10.1029/2006GL028037.

Cai, W., G. Shi, T. Cowan, D. Bi, and J. Ribbe (2005a): The response of the Southern Annular Mode, the East Australian Current, and the southern mid-latitude ocean circulation to global warming. *Geophys. Res. Lett.*, *32 (23)*: L23706, doi:10.1029/2005GL024701.

Cai, W., H. H. Hendon, and G. Meyers (2005b), An Indian Ocean Dipole in the CSIRO coupled climate model. *J. Clim.*, *18*, 1449–1468.

Chambers, D. P., B. D. Tapley, and R. H. Stewart (1999), Anomalous warming in the Indian Ocean coincident with El Nio. *J. Geophys. Res.*, *104*, 3035–3047.

Nicholls, N., B. Lavery, C. Frederiksen, W. Drosdowsky and S. Torok (1996), Recent apparent changes in relationships between the El Niño-Southern Oscillation and Australian rainfall and temperature. *Geophys. Res. Lett.*, *23*, 3357–3360.

194 Meneghini, B. I., I. Simmonds, and I. N. Smith (2006), Association between Australian
195 rainfall and the Southern Annular Mode. *Int. J. Climatol.*, *27*, 109–121.
196 Qiu, B., and S. Chen (2006), Decadal variability in the formation of the North Pacific
197 Subtropical Mode Water: Oceanic versus atmospheric control. *J. Phys. Oceanogr.*, *36*,
198 1365–1380.
199 Raphael, M. N., and M. M. Holland (2006), Twentieth century simulation of the southern
200 hemisphere climate in coupled models. Part 1: large scale circulation variability. *Clim.*
201 *Dyn., 26,* 217–228.
202 Saji, N. H., B. N. Goswami, P. N. Vinayachandran, and T. Yamagata (1999), A dipole
203 mode in the tropical Indian Ocean, *Nature*, *401*, 360–363.

Figure 1. Summer rainfall changes (a) in mm day^{-1} and (b) in percentage of control climatological values. Panels (c) and (d), the same as (a) and (b) but for winter.

Figure 2. Correlation between SEA rainfall time series (averaged over 140°E-155°E, 33°S-38°S) and grid-point anomalies of (a) rainfall, (b) SST, and (c) MSLP and wind, for summer. Panels (d) - (f), the same as (a) - (c) but for winter. An absolute value greater than 0.115 is statistically significant at a 95% confidence.

Figure 3. Correlation of grid-point summer rainfall and summer SST anomalies with a time series of east coast SST, averaged over 150°E-155°E, 33°S-38°S (panels (a) and (b)), with NINO3.4 (panels (c) and (d)), and with a time series of the IO SST EOF1 (panels (e) and (f)). Panels (g) - (l), the same as (a) - (f), but for winter.

Figure 4. Correlation between MSLP EOF1 (the SAM) time series and grid-point anomalies of (a) rainfall, (b) SST, and (c) wind for summer. Panels (d) - (f), the same as (a) - (c) but for winter. In panels (c) and (f), the MSLP EOF1 pattern is shown.

Figure 5. Changes averaged over a 31-year period between 2055-2085 of (a) SST (°C) superimposed on surface wind stress, (b) MSLP (hPa), and (c) surface shortwave radiation (W m $^{-2}$) for summer. Panels (d) - (f), the same as (a) - (c), but for winter.

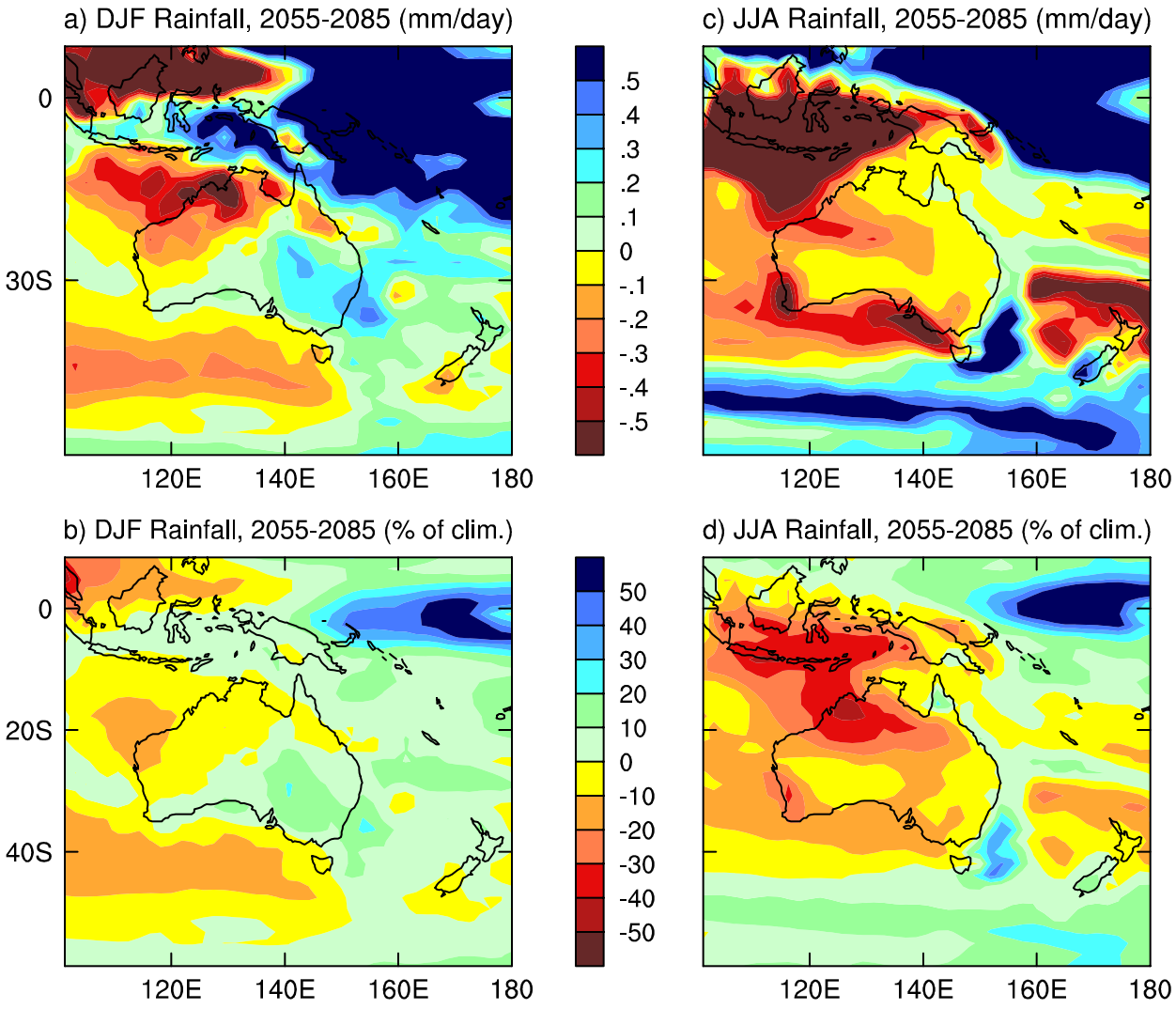
a) DJF Rainfall, 2055-2085 (mm/day)
c) JJA Rainfall, 2055-2085 (mm/day)
b) DJF Rainfall, 2055-2085 (% of clim.)
d) JJA Rainfall, 2055-2085 (% of clim.)
0
30S
20S
40S
120E
140E
160E
180
.5
.4
.3
.2
.1
0
-.1
-.2
-.3
-.4
-.5
50
40
30
20
10
0
-10
-20
-30
-40
-50

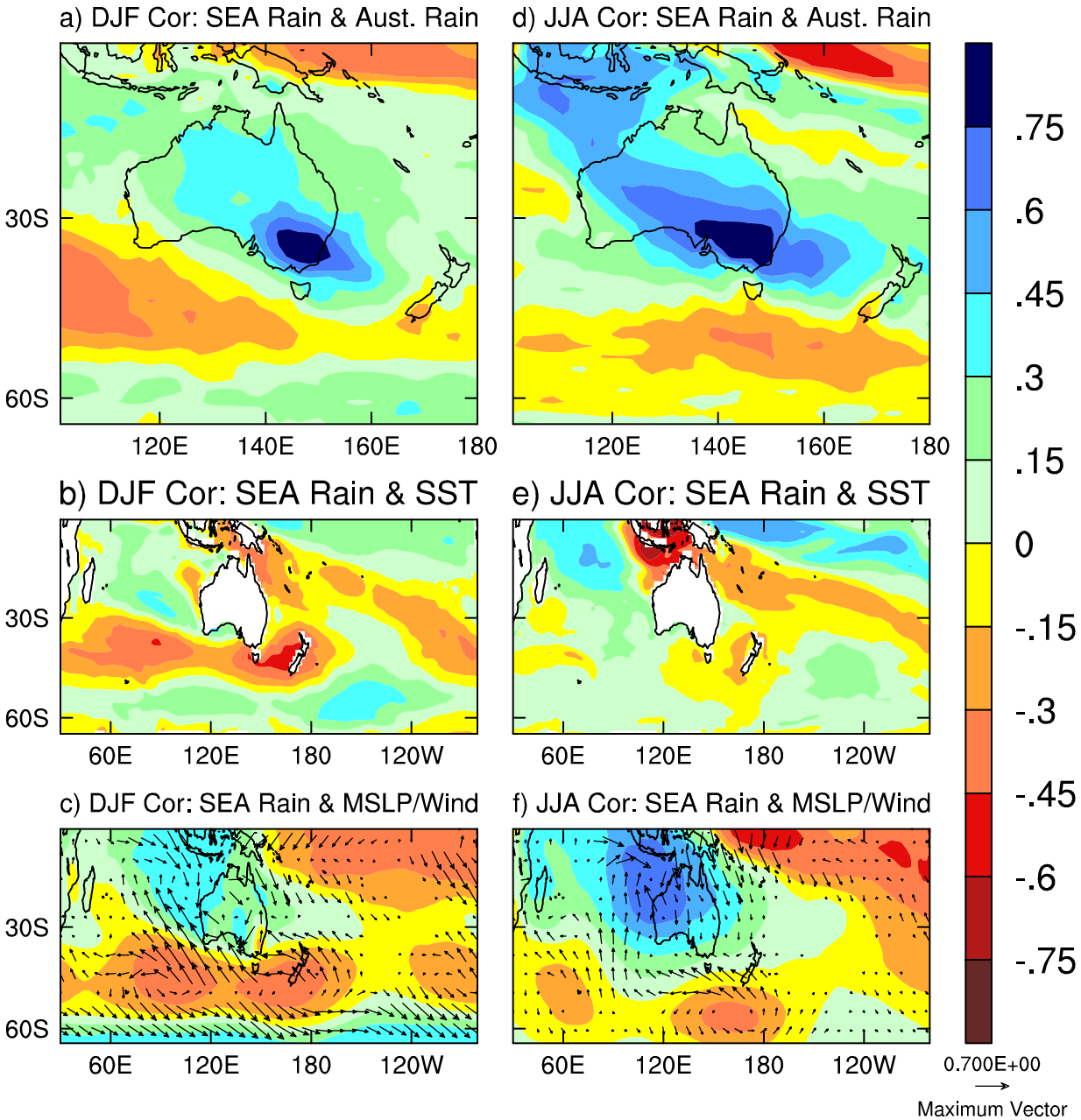
a) DJF Cor: SEA Rain & Aust. Rain
d) JJA Cor: SEA Rain & Aust. Rain
30S
60S
120E
140E
160E
180
b) DJF Cor: SEA Rain & SST
e) JJA Cor: SEA Rain & SST
60E
120E
180
120W
c) DJF Cor: SEA Rain & MSLP/Wind
f) JJA Cor: SEA Rain & MSLP/Wind
.75
.6
.45
.3
.15
0
-.15
-.3
-.45
-.6
-.75
0.700E+00
Maximum Vector

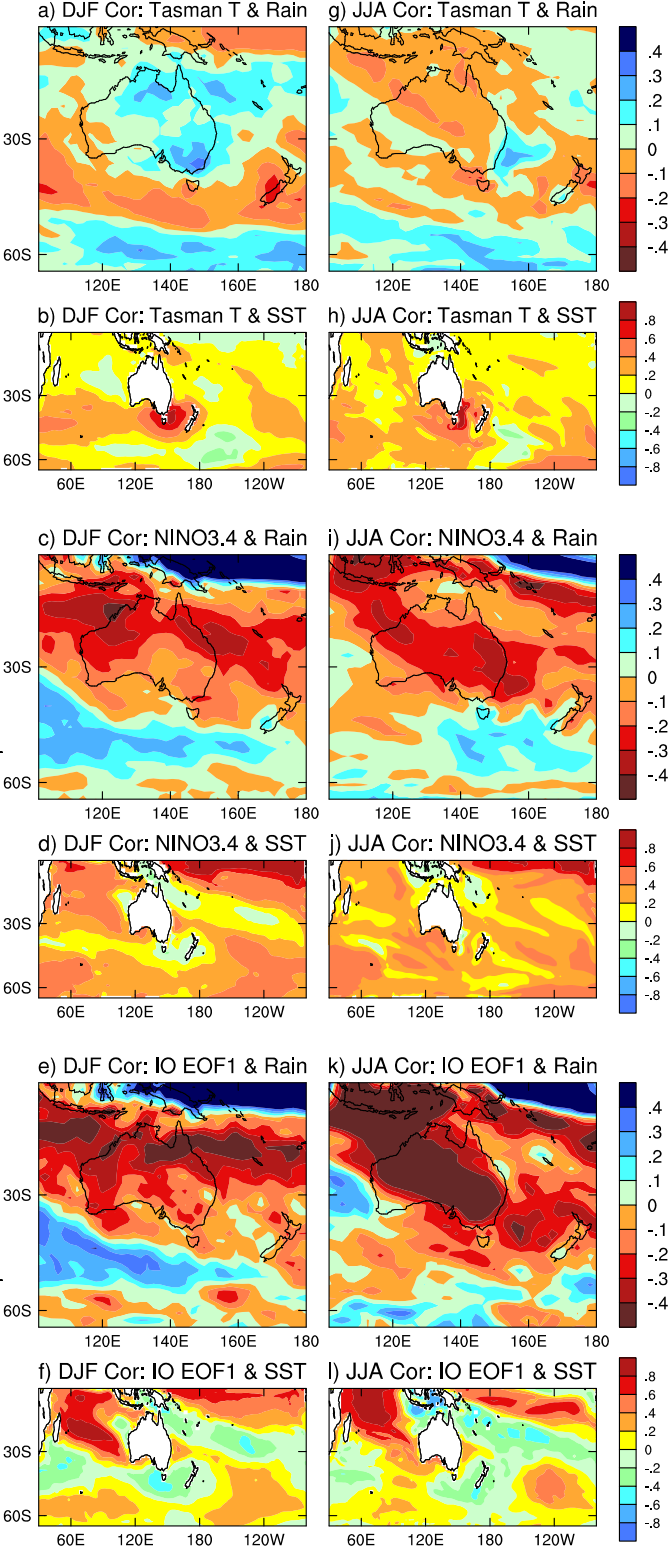
a) DJF Cor: Tasman T & Rain
g) JJA Cor: Tasman T & Rain
b) DJF Cor: Tasman T & SST
h) JJA Cor: Tasman T & SST
c) DJF Cor: NINO3.4 & Rain
i) JJA Cor: NINO3.4 & Rain
d) DJF Cor: NINO3.4 & SST
j) JJA Cor: NINO3.4 & SST
e) DJF Cor: IO EOF1 & Rain
k) JJA Cor: IO EOF1 & Rain
f) DJF Cor: IO EOF1 & SST
l) JJA Cor: IO EOF1 & SST
30S
60S
120E
140E
160E
180
60E
120W
.4
.3
.2
.1
0
-.1
-.2
-.3
-.4
.8
.6
.4
.2
0
-.2
-.4
-.6
-.8

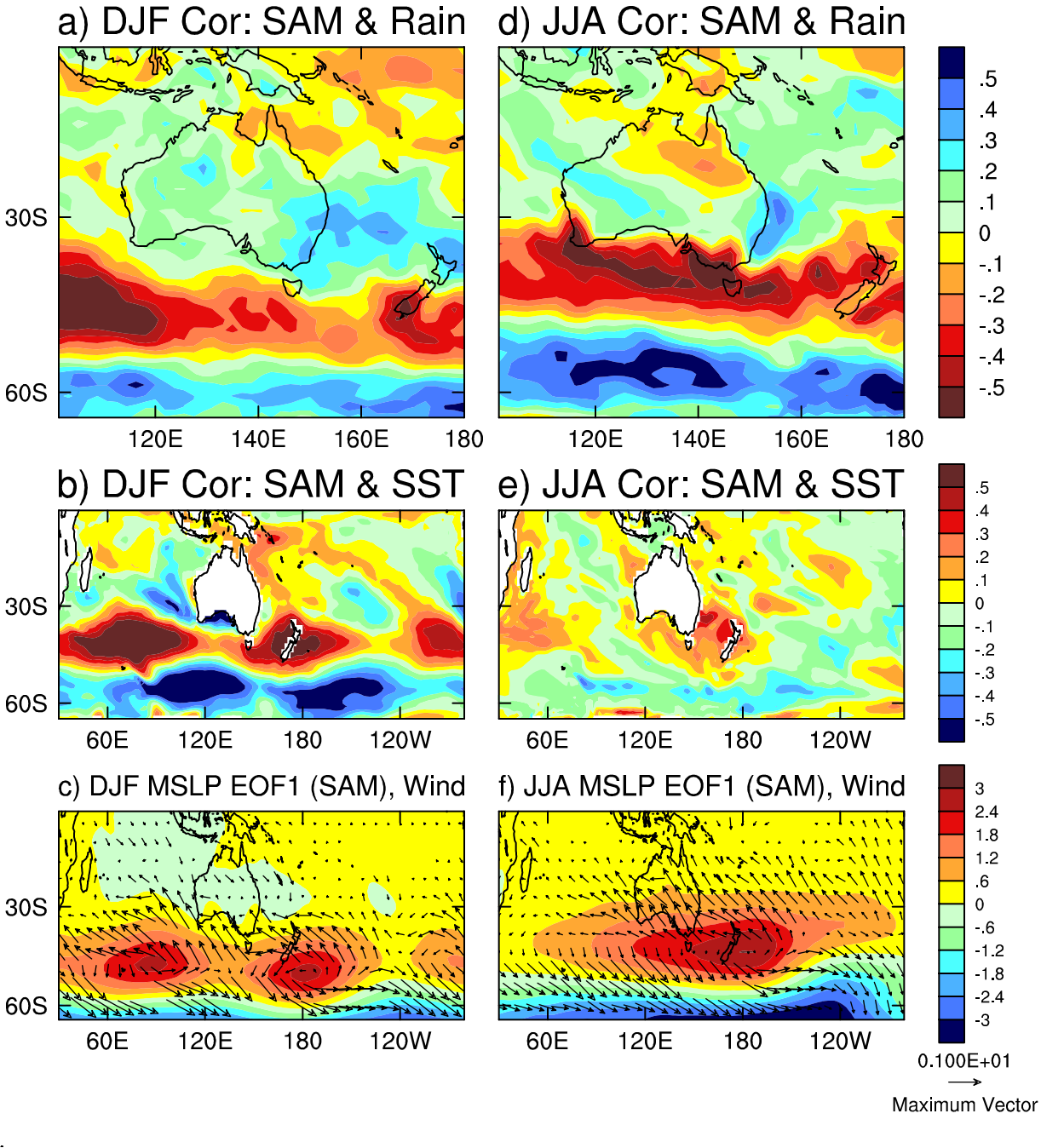
a) DJF Cor: SAM & Rain
d) JJA Cor: SAM & Rain
30S
60S
120E
140E
160E
180
.5
.4
.3
.2
.1
0
-.1
-.2
-.3
-.4
-.5
b) DJF Cor: SAM & SST
e) JJA Cor: SAM & SST
60E
120E
180
120W
c) DJF MSLP EOF1 (SAM), Wind
f) JJA MSLP EOF1 (SAM), Wind
3
2.4
1.8
1.2
.6
0
-.6
-1.2
-1.8
-2.4
-3
0.100E+01
Maximum Vector

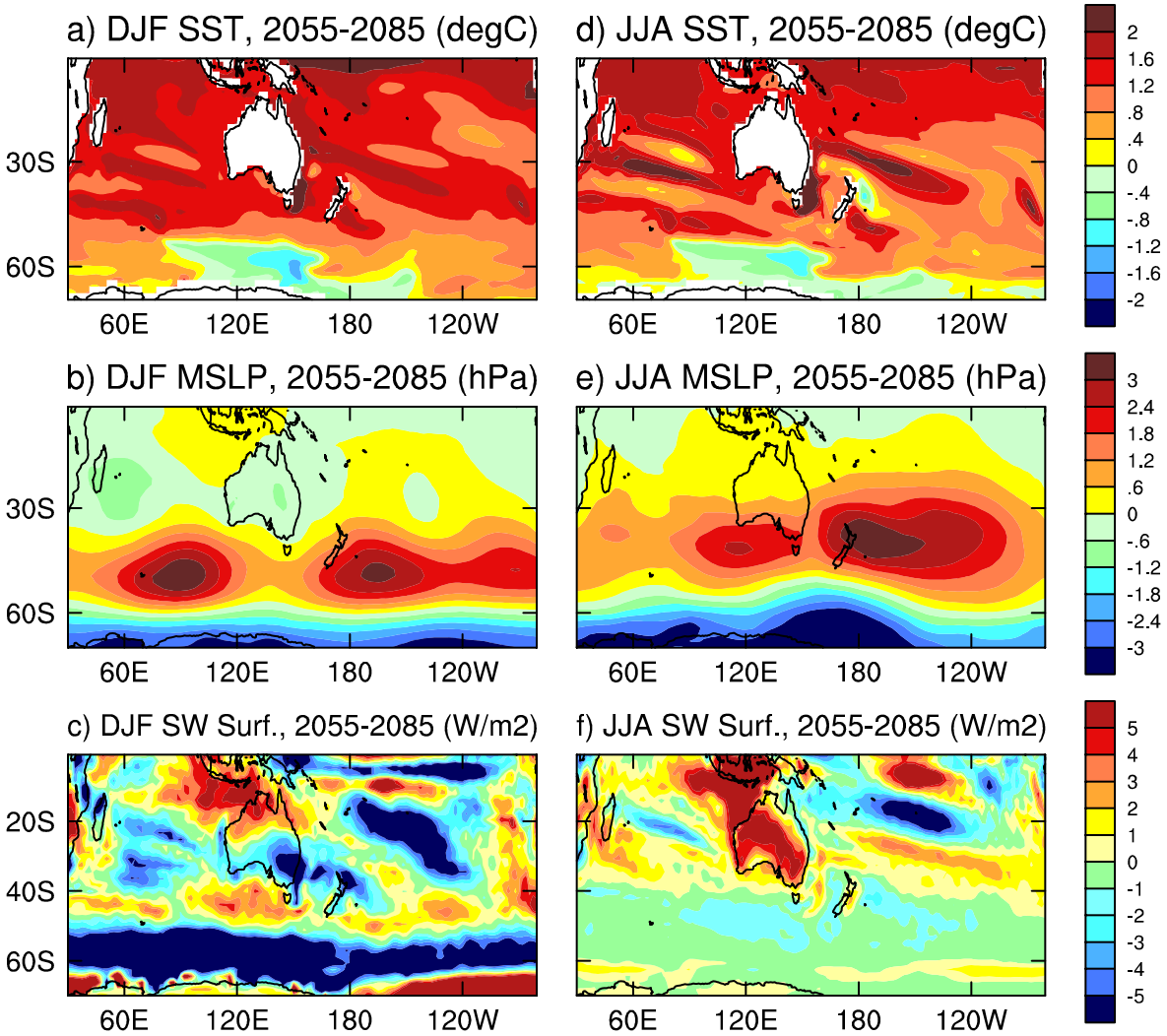
a) DJF SST, 2055-2085 (degC)
d) JJA SST, 2055-2085 (degC)
2
1.6
1.2
.8
.4
0
-.4
-.8
-1.2
-1.6
-2
30S
60S
60E
120E
180
120W
b) DJF MSLP, 2055-2085 (hPa)
e) JJA MSLP, 2055-2085 (hPa)
3
2.4
1.8
1.2
.6
0
-.6
-1.2
-1.8
-2.4
-3
c) DJF SW Surf., 2055-2085 (W/m2)
f) JJA SW Surf., 2055-2085 (W/m2)
5
4
3
2
1
0
-1
-2
-3
-4
-5
20S
40S
60S